PCATMIP: Enhancing Signal Intensity in Diffusion-Weighted Magnetic Resonance Imaging

V. M. Pai,[1]* S. Rapacchi,[2] P. Kellman,[1] P. Croisille,[2] and H. Wen[1]

Diffusion-weighted MRI studies generally lose signal intensity to physiological motion, which can adversely affect quantification/diagnosis. Averaging over multiple repetitions, often used to improve image quality, does not eliminate the signal loss. In this article, PCATMIP, a combined principal component analysis and temporal maximum intensity projection approach, is developed to address this problem. Data are first acquired for a fixed number of repetitions. Assuming that physiological fluctuations of image intensities locally are likely temporally correlated unlike random noise, a local moving boxcar in the spatial domain is used to reconstruct low-noise images by considering the most relevant principal components in the temporal domain. Subsequently, a temporal maximum intensity projection yields a high signal-intensity image. Numerical and experimental studies were performed for validation and to determine optimal parameters for increasing signal intensity and minimizing noise. Subsequently, a combined principal component analysis and temporal maximum intensity projection approach was used to analyze diffusion-weighted porcine liver MRI scans. In these scans, the variability of apparent diffusion coefficient values among repeated measurements was reduced by 59% relative to averaging, and there was an increase in the signal intensity with higher intensity differences observed at higher *b*-values. In summary, a combined principal component analysis and temporal maximum intensity projection approach is a postprocessing approach that corrects for bulk motion-induced signal loss and improves apparent diffusion coefficient measurement reproducibility. Magn Reson Med 65:1611–1619, 2011. © 2010 Wiley-Liss, Inc.

Key words: principal component analysis; diffusion; temporal MIP; low SNR

Diffusion-weighted MRI (DWI) studies generally lose signal intensity (SI) to physiological motion, which can adversely affect quantification and diagnosis. Averaging over multiple repetitions, often used to improve image quality, does not eliminate the signal loss. In DWI, physiological movement of anatomical features can be corrected for with nonrigid-body registration software packages (1–3). However, bulk motion also causes phase shifts and phase dispersion in image voxels, which never repeat precisely, leading to fluctuating intensity losses (4–6). The intensity fluctuations are smoothed out when averaging approaches are used; hence, although an increased signal-to-noise ratio is achieved, the local SI is dampened. This gets trickier at higher *b*-values where the motion sensitivity of the pulse sequence is particularly high, resulting in erroneous diffusivity values and potentially incorrect clinical diagnosis.

Principal component analysis (PCA) is a mathematical approach that helps reduce the dimensionality of the data by expressing it as a linear combination of its basis vectors (7). The first principal component accounts for a large percentage of the variability in the data, and each succeeding component accounts for as much of the remaining variability as possible. Typically, one to two principal components are sufficient to characterize an entire dataset (7). Although the utility of PCA for MR imaging has been discussed as early as 1987 (8), its primary usefulness over the last decade has been for isolating activation signals in functional MRI (9–12). Although most of these methods have been global in implementation over the entire set of images, localized approaches have been presented (12) for voxel-by-voxel analysis.

One of the first non-neurological implementations of PCA in MRI was by Wedeen et al. (13) who used it to quantitatively characterize cardiac mechanical synchrony from a time series of myocardial strain rates. Lately, PCA has been used in MRI for improving image contrast for segmentation purpose (14), analyzing diffusion tensor data (15), and for dynamic contrast-enhanced MRI studies (16,17).

Temporal maximum intensity projections (TMIPs) are performed by obtaining maximum intensity projections in the time domain for each pixel in the image space. One of the first uses of TMIP for MRI analysis was by Breeuwer et al. (18) who used TMIP to aid in drawing myocardial boundaries for registering perfusion data. Cebral et al. (19) used TMIP for developing volumetric magnitude images by taking maximum intensity of each voxel during the cardiac cycle.

The basic idea of a combined principal component analysis and temporal maximum intensity projection approach (PCATMIP) is that when the same DWI acquisition is repeated over time, the signal at each pixel fluctuates because of several factors. First is the physical movement of the anatomical features due to physiological motion. This can be effectively corrected for with nonrigid-body image registration (1–3). However, intensity fluctuation still exists because of two other factors: bulk motion-induced intensity drops and random noise. We need to reduce or remove the random noise so as to be able to pick out the maximum signal and regard it as the one with minimum motion-induced loss. For this, we exploit the fact that physiological motion is mostly cardiac and respiratory, which is mechanically transmitted to other areas. Although

[1]Laboratory of Cardiac Energetics, NHLBI, National Institutes of Health, Bethesda, Maryland, USA.

[2]CREATIS-LRMN, Institut National des Sciences Appliquées de Lyon, Lyon, France.

*Correspondence to: Vinay M. Pai, PhD, Room B1D-416, MSC 1061, LCE, NHLBI, NIH, Bldg. 10, 9000 Rockville Pike, Bethesda, MD 20892-1061.
E-mail: paiv@mail.nih.gov

Received 6 May 2010; revised 28 October 2010; accepted 7 November 2010.

DOI 10.1002/mrm.22748
Published online 16 December 2010 in Wiley Online Library (wileyonlinelibrary.com).

some organs have active peristaltic motion, these are slow and temporally coordinated in nature. Therefore, motion-induced signal fluctuations in neighboring pixels are temporally correlated, whereas random noises are not.

With this in mind, we look at a neighborhood defined by a boxcar and determine through PCA how many independent temporal behaviors (modes) are present. We then determine how many of these have amplitudes that exceed the random noise threshold and therefore represent real physiological fluctuations. If we include only these modes in reconstructing the signals in the boxcar, random noise will be reduced. In the case where only one significant mode exists in a boxcar, the procedure is equivalent to taking the temporal fluctuation of the average signal in the boxcar as the motion behavior. However, as will be shown below, more than one type of motion may exist in a boxcar. A further consideration is that the size of the boxcar needs to be large enough to distinguish coordinated physiological effects from random noise, while small enough to capture local pattern of motion-induced fluctuation. The mathematical formulation and optimization of this approach is detailed below.

PCATMIP Procedure

We first acquire a set of 2D raw images $I(x, y, m)$, where $m = 0,1,\ldots N-1$ is the number of repetitions of the 2D acquisition. For a localized operation, the set of images can be divided into subregions or boxcars, $I_{bc}(a, b, m)$, where $0 < a \leq 23$ and $0 < b \leq 23$. The Hermitian matrix is calculated over the boxcar

$$H(m,n) = \iint I^*_{bc}(a,b,m)\, I_{bc}(a,b,n)\, da\, db. \quad [1]$$

Diagonalizing the Hermitian yields the eigenvalues ε_j and eigenvectors $V_j(m)$ such that

$$\sum_m V^*_i(m)\, V_j(m) = \delta_{ij}, \quad [2]$$

where δ_{ij} is the Kronecker delta. Using these eigenvectors, the principal components $P_j(a, b)$ are calculated over the subregion:

$$P_j(a,b) = \sum_m I(a,b,m)\, V^*_j(m) \quad [3]$$

such that

$$\iint P_i(a,b) P_j(a,b)\, da\, db = \delta_{ij}\varepsilon_i. \quad [4]$$

Using a limited number f of principal components (determined by thresholding above noise floor detailed below, typically $f = 1$ or 2), the new image is calculated for the subregion as:

$$I'(a,b,m) = \sum_{k=0}^{f-1} P_k(a,b)\, V_k(m). \quad [5]$$

The pixels surrounding the pixel being interrogated are weighted to enable edge-preserving processing. If the center pixel of the boxcar is (x_c, y_c), then for any pixel (x, y) within the boxcar, the weighting is given by:

$$w(x,y|x_c,y_c) = \begin{cases} C\dfrac{1-\alpha}{r^2} & (\text{for } r \neq 0) \\ \alpha & (\text{for } r = 0) \end{cases}, \quad [6]$$

where C is a normalization factor, $\alpha \in [0, 1]$ (typically greater than 0.75), and r is the distance between pixels (x_c, y_c) and (x, y). For each pixel (x, y) in the image, the final intensity is determined by:

$$I''(x,y,m) = \frac{\sum_{\text{all}(x_c,y_c)\text{within}} w(x,y|x_c,y_c)\, I'(x,y,m|x_c,y_c)}{\sum_{\text{all}\,(x_c,y_c)\,\text{within box}} w(x,y|x_c,y_c)} \quad [7]$$

Subsequently, a pixel-wise TMIP operation yields the final image $\Theta(x, y)$:

$$\Theta(x,y) = \underset{m=0}{\overset{N-1}{\text{MAX}}}(I''(x,y,m)). \quad [8]$$

Determining the Number of Principal Components to Select

In any subregion, the number of principal components to be used can be determined by accepting the eigenvalues ε_I that are greater than the noise threshold:

$$\varepsilon_I > \beta\langle\varepsilon\rangle_{N-a}, \quad [9]$$

where β is the threshold multiplier for the eigenvalues determined in simulation and imaging experiments as detailed below, $\langle\ \rangle$ implies averaging, and a is the number of eigenvalues that have been selected to be accepted.

SIMULATIONS AND EXPERIMENTS

Numerical Simulations

If one assumes that there are at most two independent temporal patterns in a boxcar, then for a given signal-to-noise ratio (SNR) of raw data, a pair of questions arise: (a) How large should the boxcar be to minimize RMS errors, and (b) For what value of the threshold multiplier, β, will the correct number of principal components get chosen?

To validate PCATMIP and to answer these questions, we have used two different numerical phantoms (implemented with SNR of 5, unless noted otherwise), as shown in Fig. 1:

a. A uniform SI phantom with added-in fluctuation.
b. A phantom with two nonoverlapping zones with the intensities of the two zones fluctuating independently.

The uniform phantom evaluated the selection of one principal component, whereas the phantom with two nonoverlapping zones evaluated the selection of two principal components. Experimentally acquired porcine liver diffusion data were used to generate the SI fluctuation. Regions-of-interest were drawn on the liver and adjacent organ on motion-registered images, and the average signal in these ROIs over the 10 repetitions was used. For

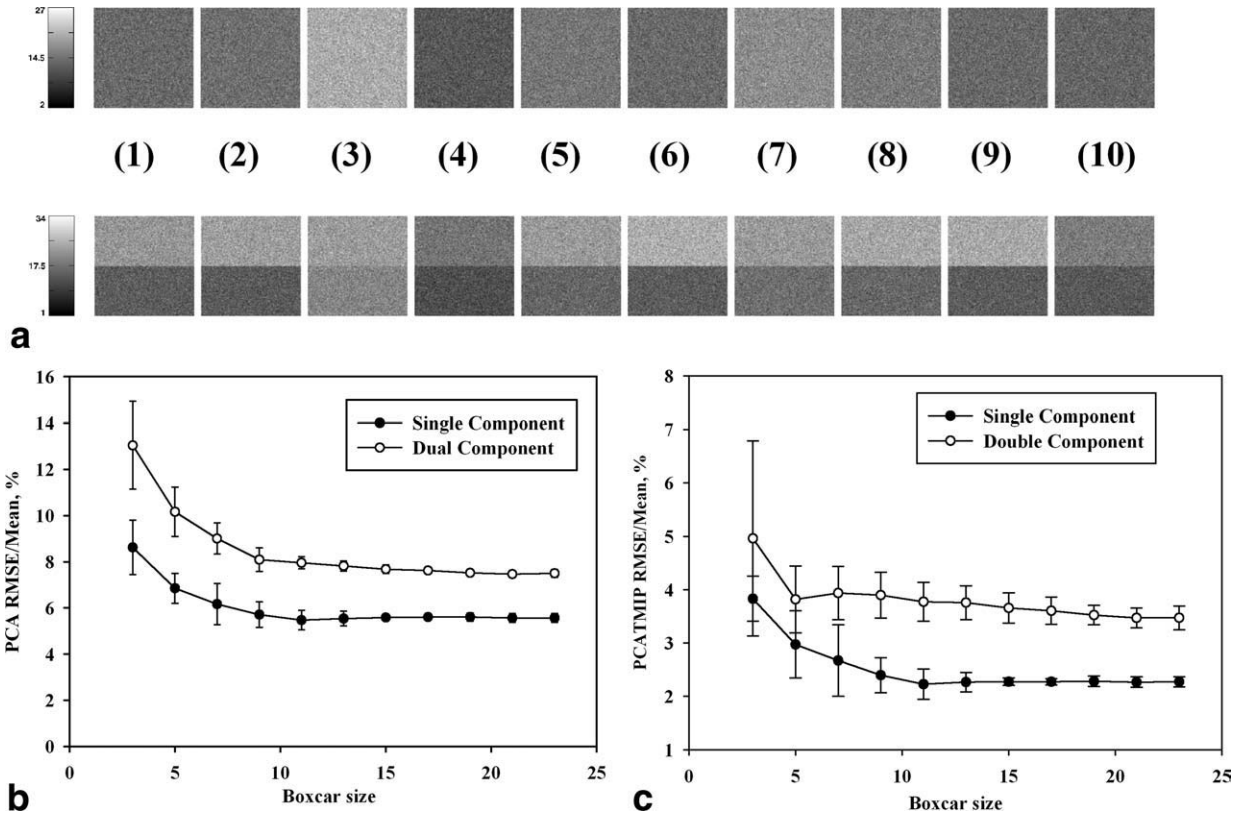

FIG. 1. **a**: Ten repetitions of uniform (top) and two zones (bottom) fluctuating numerical phantoms with Rician noise added in. **b**: The root-mean-squared error (RMSE) of the PCA-filtered signal at all time points relative to the true signal. **c**: The RMSE of the peak signal obtained with PCATMIP relative to the true peak signal.

the uniform SI phantom (i.e., liver ROI), the relative level of fluctuation was 15.4%, whereas for the two nonoverlapping zones, the levels were 14 and 11%. The uniform phantom with zero SI was used to determine the optimal range for β, the noise threshold multiplier. Subsequently, PCATMIP processing is performed on the entire image using the optimal boxcar size for the sliding window implementation to evaluate SNR variation.

For determining the effectiveness of the PCATMIP approach, the following error measures were used:

i. Root-mean-squared-error ($RMSE_I$) of the processed image intensities of all repetitions

$$\mathrm{RMSE_I} = \sqrt{\sum_{x,y,t}\left[\frac{\left(I'_s(x,y,t) - I(x,y,t)\right)^2}{S_b * S_b * N_t}\right]} \quad [10]$$

ii. Root-mean-squared-error ($RMSE_p$) of the maximum intensity

$$\mathrm{RMSE_p} = \sqrt{\sum_{x,y}\left[\frac{\left(\Theta'_s(x,y) - \Theta(x,y)\right)^2}{S_b * S_b}\right]} \quad [11]$$

For all the scenarios, the phantom was 128 × 128 pixels, and 10 images with intensity fluctuations were generated ($N_t = 10$). A range of square boxcar sizes ($S_{b,min} = 5$ and $S_{b,max} = 23$, in steps of 2) were implemented to evaluate the PCATMIP approach and to determine optimal boxcar sizes. Two different random noise variants were considered: (a) normally distributed and (b) Rician noise. As Rician noise introduces amplitude offset to the data, the thresholds for accepting eigenvalues will be different for Rician and normally distributed data. However, most clinical MRI studies yield absolute data (rather than complex data), for which the noise is Rician in nature, and hence, the subsequent analysis only considers this noise form. For scenarios where complex data (i.e., real and imaginary components) can be recovered (20) or is available for the DICOM-format DWI images, the analysis for normally distributed noise is presented in the Appendix.

The Rician-distributed noisy intensity images were generated as:

$$I'(x,y,t) = \sqrt{I_r^2(x,y,t) + I_i^2(x,y,t)} \quad [12]$$

wherein

$$I_r(x,y,t) = I(x,y,t) + G_1(\sigma)$$
$$I_i(x,y,t) = G_2(\sigma)$$

and $G(\sigma)$ is Gaussian noise with zero mean and standard deviation, σ:

$$\sigma = \frac{\overline{I(x,y,t)}}{\mathrm{SNR}} \quad x,y \in [0,\ S_{b,max}]. \quad [13]$$

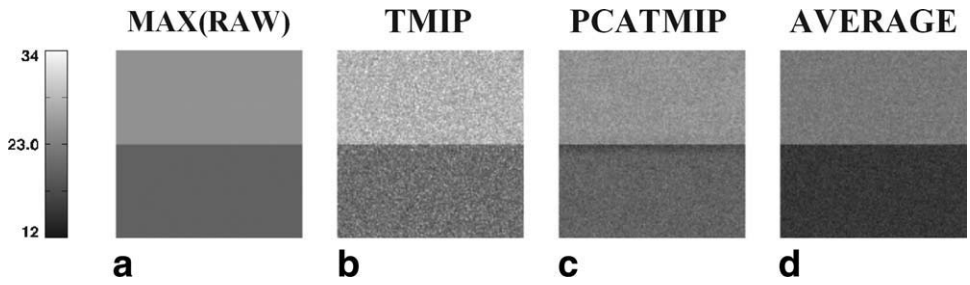

FIG. 2. Evaluation of the entire two-zone phantom for SNR of 6 shown in Fig. 1. **a**: The true, noiseless image. **b–d**: Phantom reconstruction using TMIP, PCATMIP, and averaging operations. All images are windowed to the same level illustrated by the grayscale bar.

For the two nonoverlapping zones phantom, the PCATMIP simulation was first performed on a central region straddling the two zones, with the maximum size of 23 × 23 (i.e., $S_{b,max}$), and subsequently, the PCATMIP process was performed on the entire set of images using the optimal values for the sliding window implementation. For this Rician noise phantom, we used a SNR of 6 (achieved for $b = 800$ sec/mm^2 diffusion images on our 1.5-T MRI scanner).

Experimental Study

Several experiments were performed on a 1.5-T clinical Siemens Avanto MRI scanner (Siemens Medical Solutions, Iselin, NJ) to verify the PCATMIP approach:

a. A noise image was acquired in absolute mode using a FLASH sequence.
b. A static water/agarose phantom was used to acquire diffusion-weighted images.
c. A porcine model was used to acquire diffusion images under physiological conditions.

For all scans, vendor-supplied pulse sequences were used. A monopolar, diffusion-weighted 2D echo-planar imaging sequence was used for imaging the water/agarose phantom as well as for the porcine study. For the animal study, a Yorkshire pig (male, 29 kg) was used in accordance with Animal Care and Use Committee regulations under an approved animal use protocol. The animal was anesthetized using isoflurane, and its breathing was controlled with a respirator. The echo-planar imaging sequence was used with the following parameter: *b*-values of 0, 200, 400, and 800 sec/mm^2, echo time: 68 msec, pulse repetition time: 5 sec, parallel imaging rate 2 using GRAPPA, 6/8th partial Fourier, slice thickness: 6 mm, field of view: 320 × 252 mm^2, and in-plane resolution: 2 × 2 mm^2/pixel.

Ten repetitions of the DWI sequence were used to acquire 18 slices in transverse and coronal directions during free breathing. Also, to test the stability of the PCATMIP method, we acquired 40 repetitions of the DWI sequence under free-breathing conditions and randomly divided these into six groups of 10 repetitions. Two-dimensional nonrigid registration (2,21,22) was performed for each data set to correct for bulk motion.

Subsequently, TMIP, PCATMIP, and averaging operations were performed before obtaining the diffusion trace-weighted images and generating apparent diffusion coefficient (ADC) maps. SI and SNRs were determined using these approaches and used to evaluate the effectiveness of TMIP and PCATMIP approaches relative to averaging.

RESULTS

Numerical Studies

Figure 1 shows RMSE plots for the single-component phantom and the dual-component phantom with Rician noise added in. For both phantoms, the RMSE of the images after PCA (Fig. 1b) stabilizes to a small value (<9%) as a percentage of the mean signal. Similarly, the RMSE for PCATMIP (Fig. 1c) is fairly low at increased boxcar sizes. For both PCA and PCATMIP, the RMSE stabilizes for boxcars bigger than 11 × 11.

Using a boxcar size of 15 × 15 and a threshold multiplier, β, value of 40, the two-zone phantom shown in Fig. 1a was processed using TMIP, PCATMIP, and averaging methods.

Figure 2 shows the results of the simulations with all the images windowed to the same level as indicated by the grayscale bar. Figure 2a shows the ideal noiseless image without image processing, whereas Fig. 2b–d shows the results after TMIP, PCATMIP, and averaging operations, respectively. Although TMIP achieves the highest SI, the PCATMIP SI is more true to the maxima of the numerical phantom (as some TMIP signal spikes represent noise). Averaging the noisy phantom yields the lowest SI of the three approaches.

Experimental Studies

The Rician noise acquisition was analyzed, and the results were compared to numerical simulations in Fig. 3. The results were plotted as a ratio of the first eigenvalue (representing the "DC component") and the last eight eigenvalues, representing the "true noise" in the noise scan. These ratios were computed over a range of boxcar sizes yielding excellent agreement between the numerical and experimental threshold values for boxcar sizes greater than 13.

Figure 4 shows the results for the water–agarose phantom. PCATMIP processing was done using a 15 × 15 boxcar and β of 40. Similar to the numerical phantom studies, the TMIP approach yields the highest SI and the least SNR at all *b*-values. PCATMIP yields a slight increase in SI of less than 1%, as expected in a static phantom. The SNR of PCATMIP is lower than that of averaging by less than 25%. With similar display windowing, the ADC maps for the agarose/water phantom between that obtained by PCATMIP and averaging are the same, and this is confirmed by the calculated ADC values of 2 × 10^{-3} mm^2/sec (23) (two-tailed *P*-value of 0.21 and 0.36 for agarose and water, respectively, by *t*-test for unequal variances using the Microsoft Excel Analysis ToolPak). The

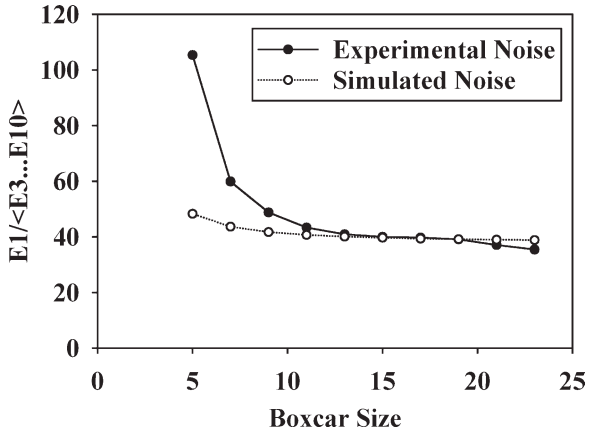

FIG. 3. Comparing experimental and simulated Rician noise for determining noise rejection threshold in the PCATMIP approach.

ADC value obtained by TMIP is smaller than that obtained by PCATMIP or averaging ($P = 0$).

Figures 5–8 show the results for the porcine liver DWI. Figure 5 summarizes the statistics over the six different sets of 10 repetitions. As in the phantom study, the PCATMIP approach yields 11–18% higher SI relative to the averaging method ($P < 0.003$ for $b = 0$ and $P < 0.001$ otherwise by two-tail t-test considering unequal variances). Although the SNR of TMIP is less than that of the averaging approach for all b-values ($P < 0.002$ by two-tail t-test considering unequal variances), the SNR of PCATMIP approaches that of averaging for all $b > 0$ ($P = 0.33$ by two-tail t-test considering unequal variances) and decreased by 16% for $b = 0$ ($P = 0.03$). Using averaging to process the six data sets, the ADC value in the liver varied by 4.1×10^{-5} mm^2/sec among the sets. In contrast, the variability was 1.7×10^{-5} mm^2/sec by the PCATMIP method, suggesting that this method minimized the variability of the ADC measurements by 59%.

Figures 6 and 7 show the trace-weighted coronal and transverse images, respectively, obtained by the three different methods for each b-value considered. Although the TMIP images show high SI at all b-values, there is a corresponding increase in noise, as evident at the higher b-values. Both figures also show that the PCATMIP and averaging approaches yield similar noise levels; however, at higher b-values, the SI in the PCATMIP images is higher than that of the averaged images. This is especially noticeable in the coronal images in the anterior dome region of the liver (higher b-values averaged images show hypointense regions). The difference in image quality between PCATMIP and averaging is also apparent in the transverse images in lateral and central areas of the liver.

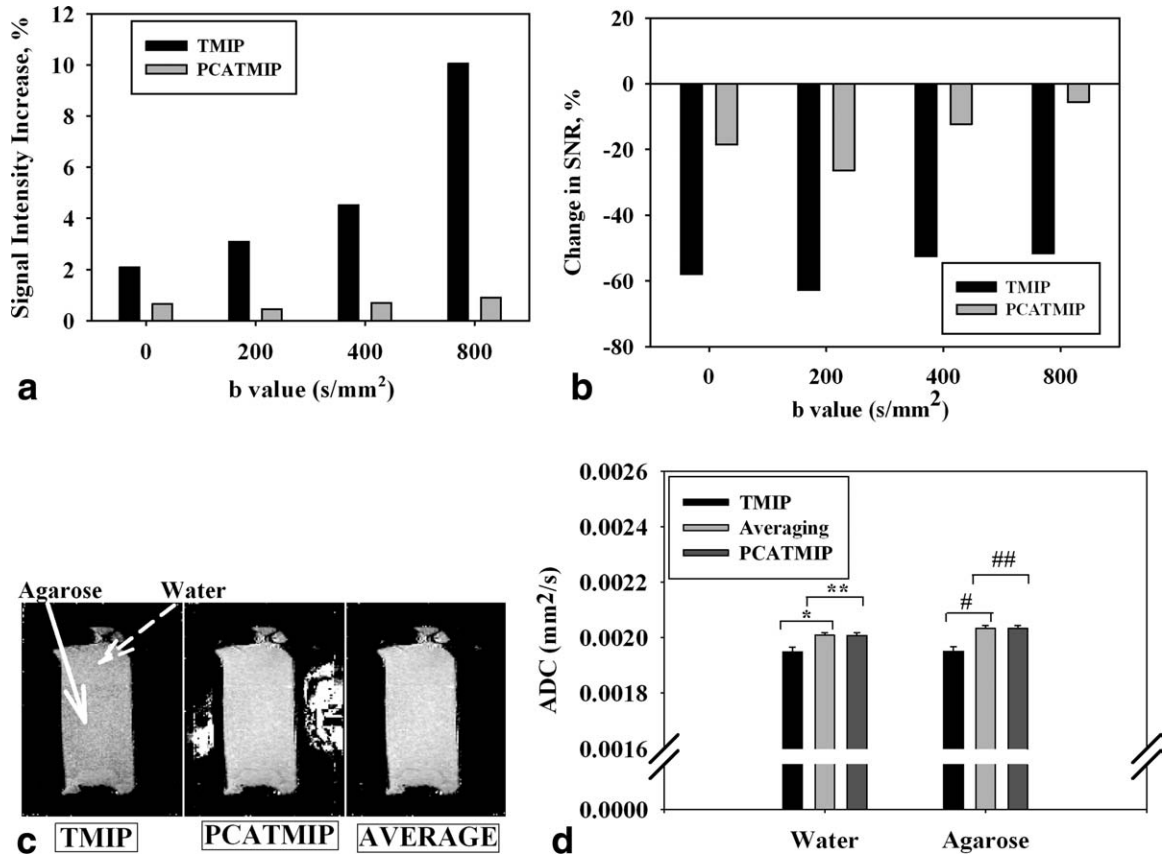

FIG. 4. Results from the static water–agarose phantom study. **a**: Increases of DW image intensity with TMIP and PCATMIP processing relative to averaging. **b**: DW image SNR changes from TMIP and PCATMIP relative to averaging. **c**: ADC maps developed by TMIP, PCATMIP, and averaging approaches. **d**: ADC values in agarose and water regions (*, #: two-tailed P value of 0 indicating nonidentical ADC means values for TMIP and averaging. **$P = 0.36$ and ##$P = 0.21$ indicating identical ADC mean values for PCATMIP and averaging).

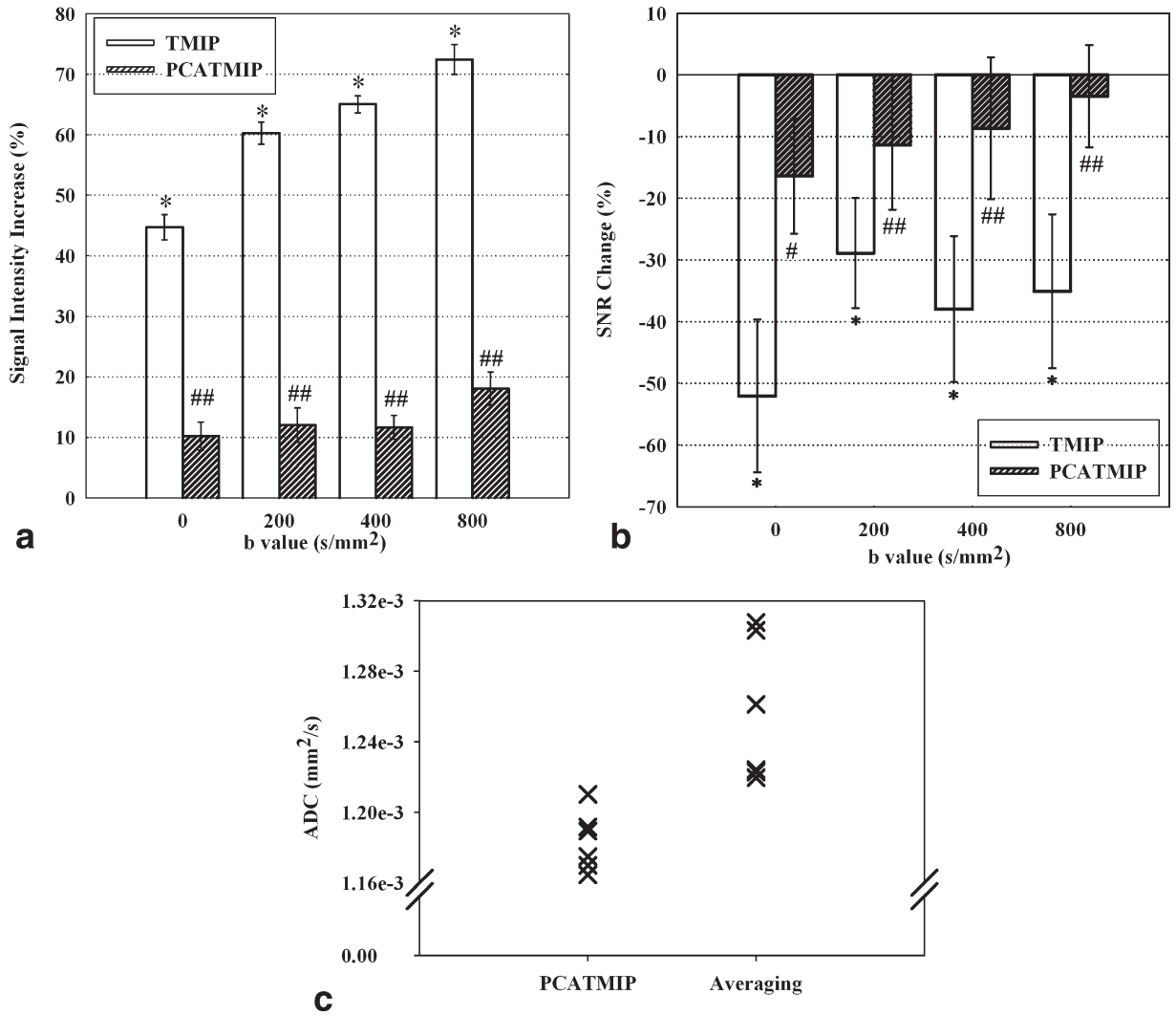

FIG. 5. Results from the porcine study. **a**: DW image intensity increases relative to averaging from TMIP and PCATMIP processing (two-tailed *P*-values using *t*-test with unequal variances were $^*P < 0.001$, $\#\#P < 0.03$ for $b = 0$ and $P < 0.001$ otherwise). **b**: DW image SNR changes from TMIP and PCATMIP relative to averaging (two-tailed *P*-values using *t*-test with unequal variances were $^*P < 0.002$ for TMIP and $\#P = 0.03$ for $b = 0$ and $\#\#P = 0.33$ for $b > 0$ for PCATMIP). In these figures, the measurements were from the liver. The error bars indicate the variability over the six groups of randomly assigned 10 repetitions each from a 40 repetitions acquisition. **c**: Variation in ADC values over the six randomly assigned data groups as determined by PCATMIP and averaging methods.

Figure 8 shows the ADC maps from representative transverse and coronal slices as well as the difference in the values obtained by the three approaches. The ADC maps from TMIP appear to be noisier than those of PCATMIP and averaging, in agreement with the SNR statistics in Fig. 5. The ADC difference between PCATMIP and averaging is positive in some areas and negative in others, indicating that the level of motion-induced signal loss in the averaging approach varies among different *b*-values and from location to location.

DISCUSSION AND CONCLUSIONS

Physiological motion-induced signal attenuation has generally affected the utility of diffusion MRI particularly for body imaging. Although image registration corrects for the physical movement of anatomical features, it does not help with the signal attenuation. Although averaging over multiple repetitions improves image SNR, it does not resolve this motion-induced signal loss issue.

An intuitive method for recovering motion-induced signal loss is to perform a pixel-wise TMIP over the multiple repetitions instead of averaging them. Ideally, this results in a DWI data set of the least amount of motion-induced signal loss. However, as TMIP assigns the pixel values of individual repetitions to the final result, noise spikes can easily be highlighted, leading to overestimation of the image intensity and high noise levels.

The PCATMIP approach achieves an optimal middle ground between averaging and TMIP. Our pig study showed that the PCA of local temporal modes allowed us to remove random noise from the physiological fluctuations before the TMIP procedure. The result was recovery of motion-induced signal loss while maintaining SNR comparable to simple averaging. The keys to

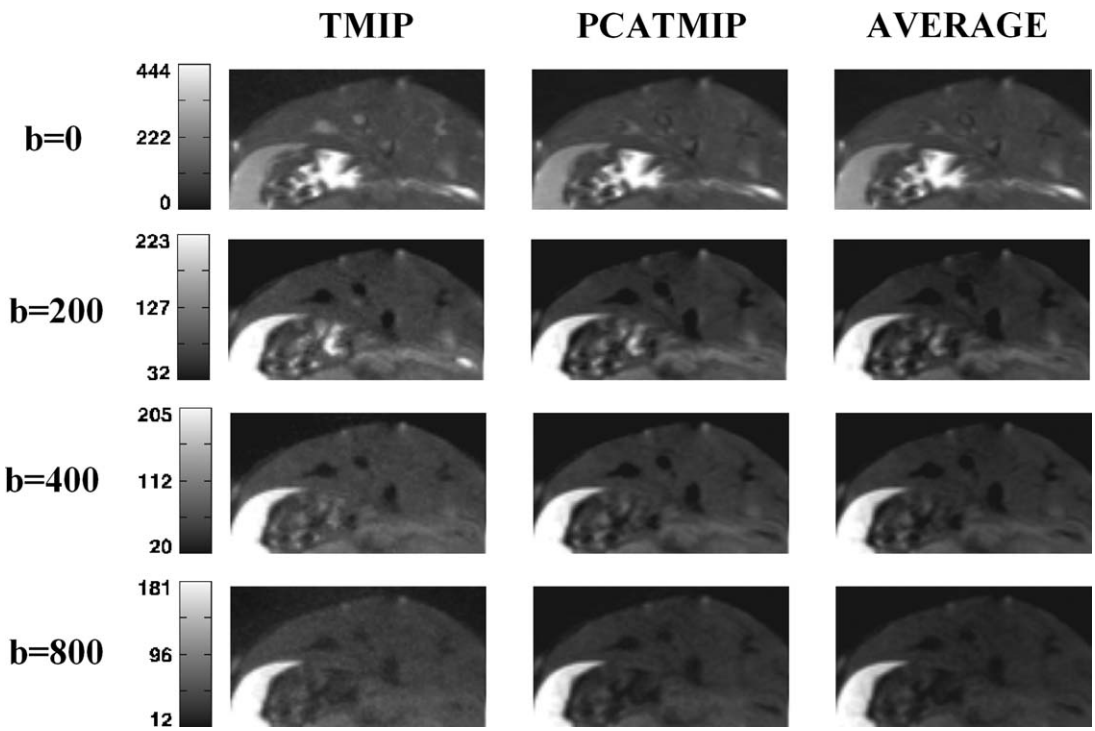

FIG. 6. Trace-weighted coronal images from a porcine DWI scan. Left: TMIP; middle: PCATMIP; right: Averaging. *b*-values used: 0, 200, 400, and 800 sec/mm^2. All images at each *b*-value were windowed identically; windowing of each *b*-value is independent of the other *b*-values to highlight differences in the image processing techniques. Note the differences in the central region of the liver.

successfully implementing PCATMIP are correctly selecting the boxcar size and identifying the threshold amplitude of the temporal modes that separates coordinated physiological fluctuations from random noise.

Simulations show that very small boxcar sizes lead to a mixing of the temporal modes that represent bulk motion with those of random noise, resulting in large errors in the estimated motion-induced fluctuations.

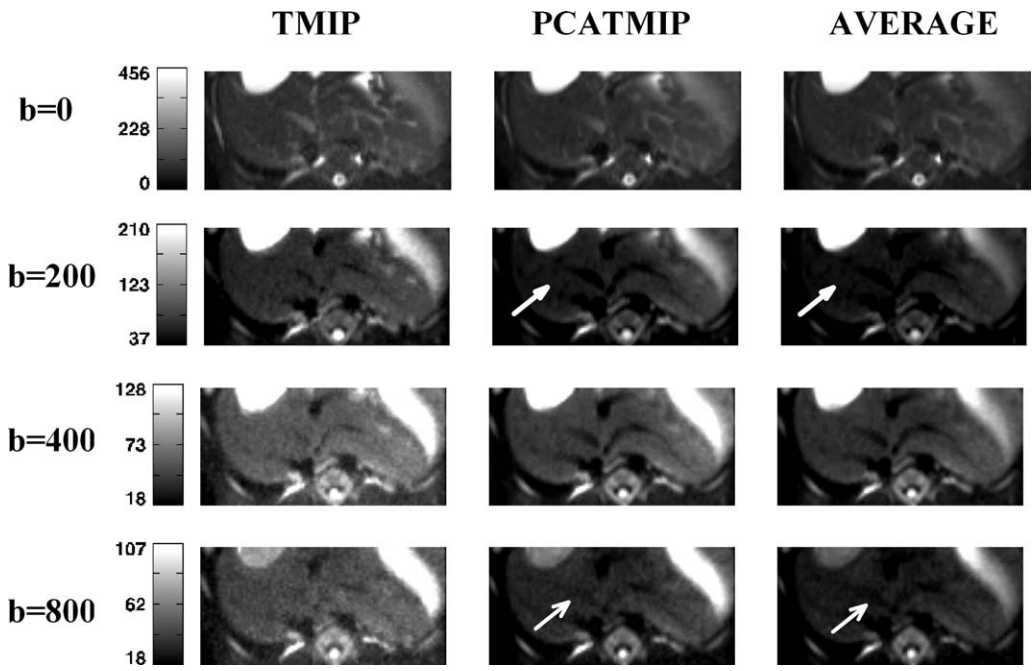

FIG. 7. Trace-weighted axial images from a porcine DWI scan. Left: TMIP; middle: PCATMIP; right: Averaging. *b*-values used: 0, 200, 400, and 800 sec/mm^2. All images at each *b*-value were windowed identically; windowing of each *b*-value is independent of the other *b*-values to highlight differences in the image processing techniques. Note the apparent higher noise level in the TMIP results and the intensity difference between PCATMIP and averaging in the liver indicated by arrows.

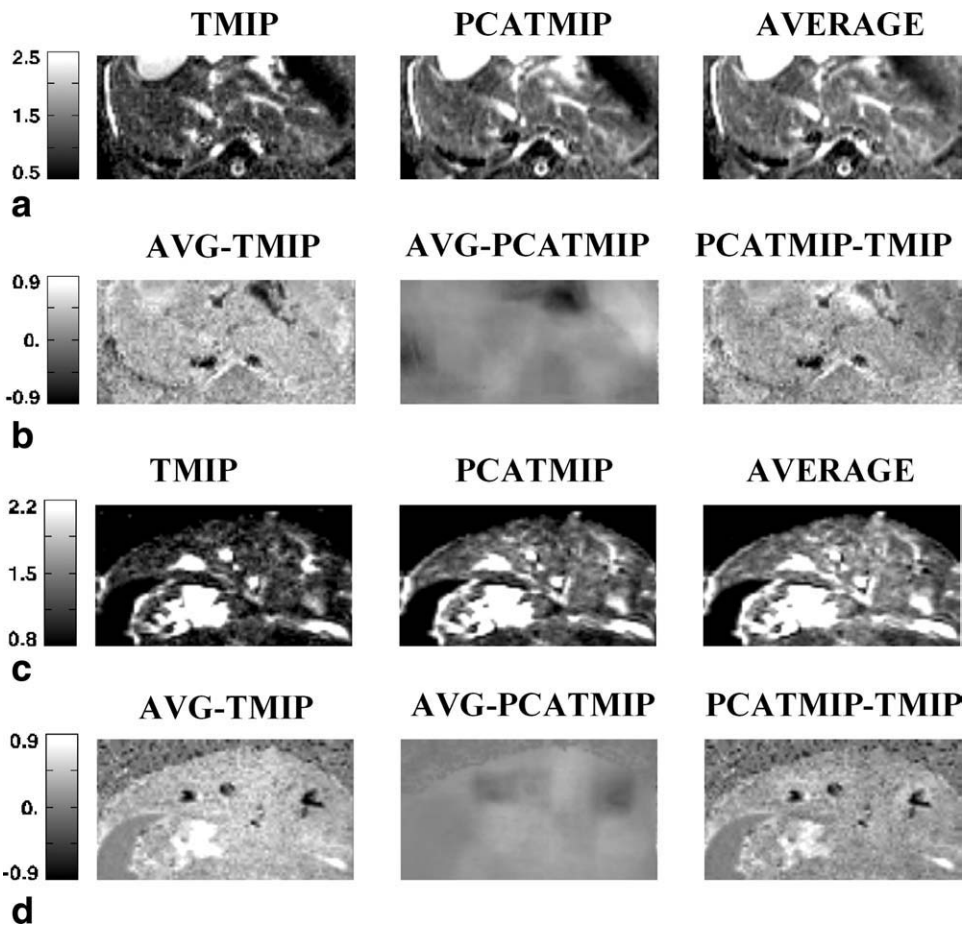

FIG. 8. ADC maps for representative transverse (**a** and **b**) and coronal (**c** and **d**) slices in porcine DWI. Images **a** and **c** show ADC maps developed by the three different approaches discussed in the article, whereas images **b** and **d** show difference in ADC values between the three approaches. All values are in units of 10^{-3} mm^2/sec.

However, too large a boxcar size may include more than two independent modes of motion, resulting in lower SNR. The optimal boxcar size should be as small as possible but large enough to avoid appreciable contamination from random noise modes. For a given boxcar size and noise distribution in the raw data, it is also essential to determine a threshold amplitude of the temporal modes which is just high enough to reject all the random noise modes. For Rician noise, where the noise is positively biased, a boxcar size of 30 mm and a threshold multiplier of 40 have been found to be a good combination. Significantly, when the incoming raw data contain both magnitude and phase, the threshold multiplier can be set much lower, as shown in the Appendix. For this reason, it is worthwhile to keep the phase information in the raw data.

Computationally, PCATMIP analysis of a three *b*-values DWI dataset acquired over 10 repetitions requires less than a minute after the nonrigid-body data registration (which also takes about a minute).

The main drawback of the PCATMIP approach is the nonattenuation or enhancement of artifactual signal, such as due to aliasing. Occasional artifactual signal is dampened by averaging but retained by the PCATMIP procedure as real signal. This can significantly affect the final image and its clinical utility.

Another drawback is the need to acquire multiple repetitions. It is more appropriate for low SNR situations where this becomes necessary regardless of the processing method.

In summary, we have developed an approach that permits the recovery of signal intensities, primarily by the suppression of the noise components of the acquired data and by maximizing the SI at each spatial point across multiple repetitions of the image acquisition. This PCATMIP approach combines the optimal aspects of averaging and TMIP operations and yields higher SI as well as higher SNRs than either operation, respectively. Due to these enhancements, this image processing approach may prove useful in extending diffusion-weighted imaging for body applications clinically.

APPENDIX: APPLICATION OF PCATMIP FOR GAUSSIAN NOISE (I.E., NON-RICIAN NOISE)

For applying the PCATMIP approach to complex data, Gaussian random noise was added to produce noisy intensity:

$$I'(x,y,t) = I(x,y,t) + d(x,y,t)$$

wherein the width of the normal distribution was

$$\text{Noise Level} = \frac{\overline{I(x,y,t)}}{\text{SNR}} x,y \in [0, S_{\text{b,max}}].$$

Similar to the Rician analysis, a range of square boxcar sizes ($S_{\text{b,min}} = 3$ and $S_{\text{b,max}} = 23$, in steps of 2) were considered. Both first and second eigenvector RMSEs were found to approach zero for boxcar sizes greater than 9.

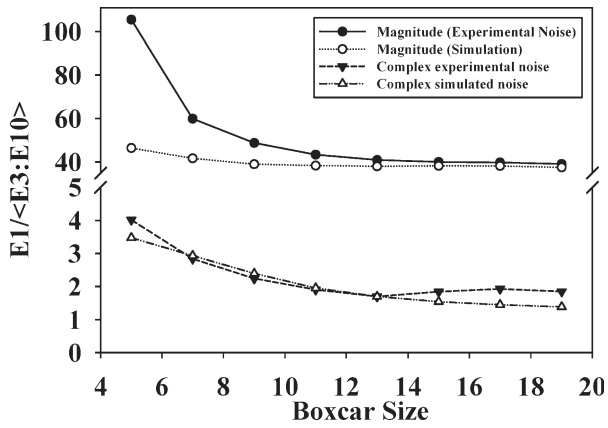

FIG. A1. Comparing experimental and simulated Rician and Gaussian noise for determining the threshold for noise rejection in PCATMIP. Both magnitude-only and complex images are considered. Complex data permit a lower threshold than magnitude-only data.

Monte Carlo simulation using a SNR of 2 was used to determine the range of boxcar sizes and threshold multiplier (β) values over which the correct number of eigenvalues was successfully determined for single-component and dual-component phantoms. These simulations show that although the effective range for β is between 1 and 60 for a single-component phantom, its range is between 1 and 8 for selecting two components for the given SNR.

Based on these results, a boxcar of 11 × 11 was further evaluated, and although the single-component phantom had a very large range over which the value of β could be chosen, the dual-component phantom was found to yield successful selection of eigenvalues for β values greater than 2 so long as SNR greater than 1 was achieved.

Finally, considering the noise-only phantom, the numerically computed results were compared to the eigenvalue ratio from the experimentally acquired noise scan (Fig. A1). Unlike the Rician noise analysis, the Gaussian noise analysis yields a lower ratio of $E1/\langle E3{:}E10\rangle$. Also, both numerically synthesized noise and the experimental scan yielded similar results for boxcar sizes greater than 10 with the ratio tending toward 2.

Based on these simulations, for a diffusion-weighted set where the complex data are readily available, PCATMIP can be successfully used with a boxcar size of 11 × 11 and a β of 2.

REFERENCES

1. Chandrashekara R, Rao A, Sanchez-Ortiz GI, Mohiaddin RH, Rueckert D. Construction of a statistical model for cardiac motion analysis using nonrigid image registration. In: Proceedings of Information Processing in Medical Imaging, Vol. 2732. Ambleside, UK; 2003. pp 599–610.
2. Chefd'hotel C, Tschumperle D, Deriche R, Faugeras O. Constrained flows of matrix-valued functions: application to diffusion tensor regularization. In: ECCV '02 Proceedings of the 7th European Conference on Computer Vision-Part I, Vol. 2350. Copenhagen, Denmark; 2002. pp 251–265.
3. ChefD'Hotel C, Tschumperle D, Deriche R, Faugeras O. Regularizing flows for constrained matrix-valued images. J Math Imaging Vis 2004;20:147–162.
4. Bihan DL, Cyril P, Alexis A, Franck L. Artifacts and pitfalls in diffusion MRI. J Magn Reson Imaging 2006;24:478–488.
5. Chenevert TL, Brunberg JA, Pipe JG. Anisotropic diffusion in human white matter: demonstration with MR techniques in vivo. Radiology 1990;177:401–405.
6. Merboldt KD, Hanicke W, Gyngell ML, Frahm J, Bruhn H. The influence of flow and motion in MRI of diffusion using a modified CE-FAST sequence. Magn Reson Med 1989;12:198–208.
7. Joliffe IT. Principal component analysis. New York: Springer Verlag; 2002.
8. Schmiedl U, Ortendahl DA, Mark AS, Berry I, Kaufman L. The utility of principal component analysis for the image display of brain lesions. A preliminary, comparative study. Magn Reson Med 1987;4:471–486.
9. Andersen AH, Gash DM, Avison MJ. Principal component analysis of the dynamic response measured by fMRI: a generalized linear systems framework. Magn Reson Imaging 1999;17:795–815.
10. Bianciardi M, van Gelderen P, Duyn JH, Fukunaga M, de Zwart JA. Making the most of fMRI at 7T by suppressing spontaneous signal fluctuations. Neuroimage 2009;44:448–454.
11. Hansen LK, Larsen J, Nielsen FÅ, Strother SC, Rostrup E, Savoy R, Lange N, Sidtis J, Svarer C, Paulson OB. Generalizable patterns in neuroimaging: how many principal components? Neuroimage 1999;9:534–544.
12. Lai S-H, Fang M. A novel local PCA-based method for detecting activation signals in fMRI. Magn Reson Imaging 1999;17:827–836.
13. Wedeen VJ, Weisskoff RM, Reese TG, Beache GM, Poncelet BP, Rosen BR, Dinsmore RE. Motionless movies of myocardial strain-rates using stimulated echoes. Magn Reson Med 1995;33:401–408.
14. Zhang Y, Goldszal A, Butman J, Choyke P. Improving image contrast using principal component analysis for subsequent image segmentation. J Comput Assist Tomogr 2001;25:817–822.
15. Papadakis NG, Zheng Y, Wilkinson D. Analysis of diffusion tensor magnetic resonance imaging data using principal component analysis. Phys Med Biol 2003;48:N343.
16. Eyal E, Badikhi D, Furman-Haran E, Kelcz F, Kirshenbaum KJ, Degani H. Principal component analysis of breast DCE-MRI adjusted with a model-based method. J Magn Reson Imaging 2009;30:989–998.
17. Melbourne A, Atkinson D, White MJ, Collins D, Leach M, Hawkes D. Registration of dynamic contrast-enhanced MRI using a progressive principal component registration (PPCR). Phys Med Biol 2007;52:5147–5156.
18. Breeuwer M, Quist M, Spreeuwers L, Paetsch I, Al-Saadi N, Nagel E. Towards automatic quantitative analysis of cardiac MR perfusion images. Int Congr Ser 2001;1230:967–973.
19. Cebral JR, Putman CM, Alley MT, Hope T, Bammer R, Calamante F. Hemodynamics in normal cerebral arteries: qualitative comparison of 4d phase-contrast magnetic resonance and image-based computational fluid dynamics. J Eng Math 2009;64:367–378.
20. Koay CG, Özarslan E, Basser PJ. A signal transformational framework for breaking the noise floor and its applications in MRI. J Magn Reson 2009;197:108–119.
21. Hermosillo G, Chefd'Hotel C, Faugeras O. Variational methods for multimodal image matching. Int J Comput Vis 2002;50:329–343.
22. Kellman P, Chefd'hotel C, Lorenz CH, Mancini C, Arai AE, McVeigh ER. Fully automatic, retrospective enhancement of real-time acquired cardiac cine MR images using image-based navigators and respiratory motion-corrected averaging. Magn Reson Med 2008;59:771–778.
23. Issa B. In vivo measurement of the apparent diffusion coefficient in normal and malignant prostatic tissues using echo-planar imaging. J Magn Reson Imaging 2002;16:196–200.